Distributed Feedback Lasers Based on $MAPbBr_3$

Neda Pourdavoud, André Mayer, Maximilian Buchmüller, Kai Brinkmann, Tobias Häger, Ting Hu, Ralf Heiderhoff, Ivan Shutsko, Patrick Görrn, Yiwang Chen, Hella-Christin Scheer and Thomas Riedl

WILEY-VCH

DOI: 10.1002/ ((please add manuscript number))

Article type: Communication

Distributed feedback lasers based on $MAPbBr_3$

*Neda Pourdavoud[1], André Mayer[2], Maximilian Buchmüller[2], Kai Brinkmann[1], Tobias Häger[1], Ting Hu[3], Ralf Heiderhoff[1], Ivan Shutsko[4], Patrick Görrn[4], Yiwang Chen[3], Hella-Christin Scheer[2], and Thomas Riedl[1]**

[1] N. Pourdavoud, K. Brinkmann, T. Häger, Dr. R. Heiderhoff, Prof. T. Riedl

Institute of Electronic Devices, University of Wuppertal, Rainer-Gruenter-Str. 21, 42119 Wuppertal, Germany, E-mail: t.riedl@uni-wuppertal.de

[2] A. Mayer, M. Buchmüller, Prof. H.-C. Scheer

Microstructure Engineering, University of Wuppertal, Rainer-Gruenter-Str. 21, 42119 Wuppertal, Germany

[3] T. Hu, Prof. Y. Chen

College of Chemistry/Institute of Polymers, Nanchang University, 999 Xuefu Avenue, Nanchang 330031, China

[4] I. Shutsko, Prof. P. Görrn

Chair of Large Area Optoelectronics, University of Wuppertal, Rainer-Gruenter-Str. 21, 42119 Wuppertal, Germany

Keywords:

hybrid halide perovskite, $MAPbBr_3$, thermal nanoimprint, distributed feedback laser, perovskite laser

The astonishing progress in the field of hybrid halide perovskite solar cells has led to impressive power conversion efficiencies beyond 22%.[1] Moreover, their intriguing optoelectronic properties render these perovskites a promising class of materials for light emitting diodes (LEDs) and lasers.[2, 3] Perovskite LEDs have recently shown notable advances with external quantum efficiencies exceeding 10%.[4, 5] Lasers as the youngest member of the family of perovskite optoelectronic devices have entered the stage hand-in-hand with the vision to create low-cost, solution processed laser diodes. A substantial amount of work has been devoted to study amplified spontaneous emission (ASE) in methylammonium lead iodide ($CH_3NH_3PbI_3$ or $MAPbI_3$).[6] Optically pumped lasing in $MAPbI_3$ has been first reported for vertical cavity resonators[7], then micro-spherical silica resonators[8], and distributed feedback (DFB) structures.[9, 10] Perovskites other than $MAPbI_3$, e.g. $MAPbX_3$ (X=Br, Cl) and $CsPbX_3$ or $FAPbX_3$ have also been explored for lasing applications. Nanowires of $MAPbCl_xBr_{3-x}$[11], $CsPbX_3$[12] and $FAPbBr_3$[13] have been studied.

For the realization of high-Q photonic resonator structures and waveguides, the perovskite active material needs to be patterned on the nanoscale with utmost control. Due to the relatively low intrinsic stability of hybrid perovskites and their susceptibility to a number of commonly used solvents, patterning via established wet-chemical lithography techniques is extremely limited.[14, 15] This shortcoming states an obstacle that so far slows down the progress in the field of perovskite photonics. Among the structural weaknesses of hybrid perovskite materials, it is important to consider that unlike conventional inorganic semiconductors, crystal binding in these materials has been found to extend beyond purely covalent/ionic bonds, but rather also includes significant contributions of van der Waals interactions among the halide atoms as well as Hydrogen bonding.[16] Hybrid perovskites can therefore be considered as “soft materials”. Only very recently, we have demonstrated that we could directly pattern the fruit-fly of hybrid perovskites, i.e. $MAPbI_3$, by thermal nanoimprint (NIL),[17] a futile endeavor with established

inorganic semiconductors like GaAs or GaN. In parallel, Wang et al. created nano-patterns for $MAPbI_3$ based photo-detectors by thermal NIL.[18]

Beyond $MAPbI_3$, perovskite gain media like $MAPbBr_3$ with a larger bandgap and an emission in the visible spectral range would be very attractive for lasing applications. Note, semiconductor lasers in the green/yellow/orange wavelength region are of great interest, as established laser diodes (based on Indium-Gallium-Nitride etc.) experience severe limits in this spectral window. $MAPbBr_3$ thin-film DFB lasers have not been reported, as of today.

In this paper, we present the first DFB lasers based on $MAPbBr_3$ thin-films. We use thermal nanoimprint to prepare linear photonic gratings with a periodicity of 300 nm into $MAPbBr_3$ active layers. We show that these imprinted gratings form a second-order DFB resonator. Upon optical excitation, these DFB resonator structures support lasing which can be tuned in the spectral region of 543.3-557.4 nm. A very low lasing threshold of 3.4 $\mu J/cm^2$ is achieved, which is indicative of the outstanding material quality of the imprinted $MAPbBr_3$ layer. In a control experiment using a flat stamp for the imprint process, we clearly evidence the re-crystallization of the $MAPbBr_3$ from an initially rough and polycrystalline thin film to a layer consisting of extended single crystals with lateral dimensions ~10 μm and a roughness that is on the order of only 0.6 nm (root-mean-square), limited by the roughness of the flat stamp. This smooth morphology is the essential key to unlock low waveguide losses and thus to afford a low threshold for lasing. Low lasing threshold levels are mandatory for future electrical operation of a perovskite laser diode.

$MAPbBr_3$ thin films have been prepared from a solution of lead acetate ($Pb(OAc)_2$) and methylammonium Bromide (CH_3NH_3Br) in dimethylformamide following a deposition protocol that can be found in the Experimental Section.

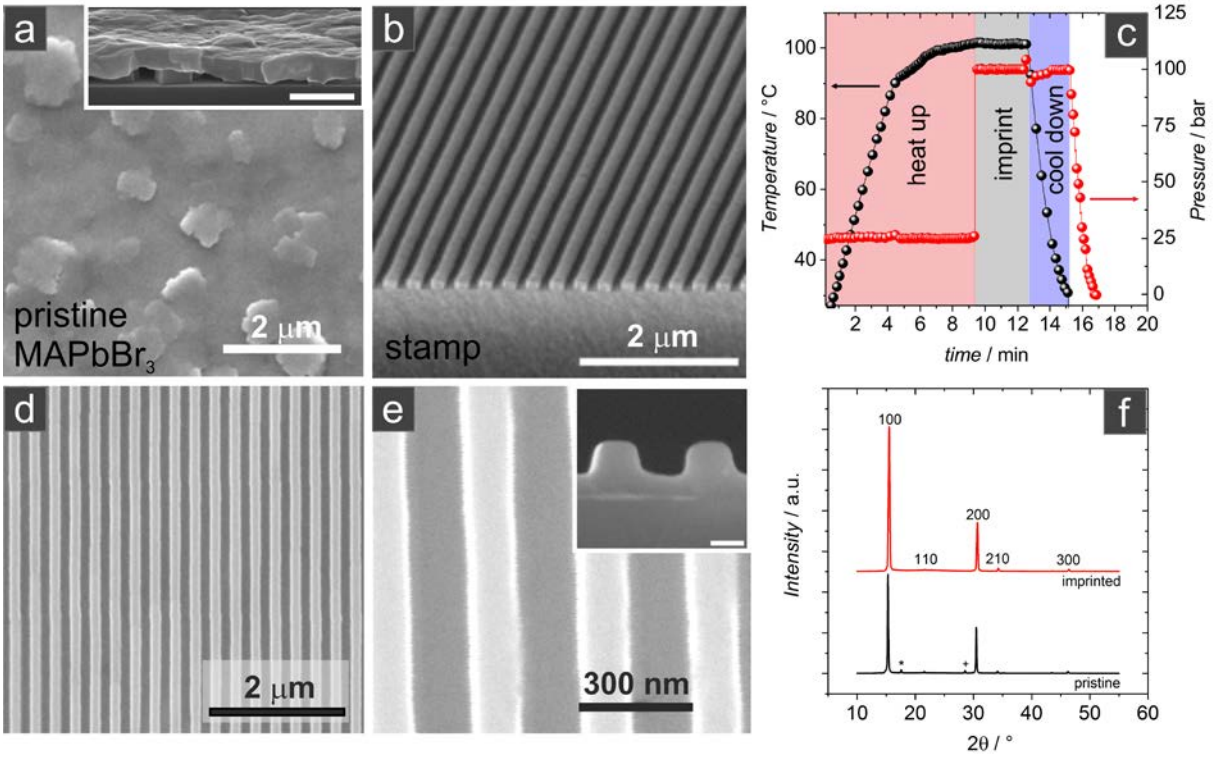

Figure 1. (a) Scanning electron microscopy (SEM) image of an as-cast $MAPbBr_3$ layer (inset: cross-section, scale bar is 1 µm). (b) NIL stamp with a linear grating with a pitch of Λ=300 nm. (c) Protocol of the imprinting process showing the temperature and pressure vs. time. (d, e) SEM images of the DFB grating imprinted into the $MAPbBr_3$ layer (inset: high resolution cross-section, scale bar is 100 nm). (f) XRD diffractograms of the pristine and imprinted perovskite layer with assignment of the most relevant peaks. A discussion of the peaks labeled (*) and (+) can be found in the text.

Figure 1a displays a SEM microscopy image of an as-cast $MAPbBr_3$ layer. The root-mean-square (rms) roughness of these layers is about 46 nm, as determined by atomic force microscopy (see **Figure 2**). The cross section of the pristine $MAPbBr_3$ layer is shown in the

inset. The stamp we used for the NIL process consists of a linear grating with a periodicity of 300 nm and a duty cycle (hill vs. valley) of 50:50 (**Figure 1b**).

The thermal imprint process followed a temperature/pressure sequence as depicted in **Figure 1c**. Further details of the NIL process can be found in the Experimental section. Essentially, we applied a pre-pressure of 25 bar before starting the heat-up procedure to the desired imprint temperature between 100°C. The duration of the imprint was 3 min. Finally, the pressure was slowly released after cooling the sample to 30°C. As can be seen in **Figure 1d,e**, the grating pattern of the stamp is perfectly replicated in the $MAPbBr_3$ layer. According to the inset in **Figure 1e**, the imprint depth is 100 nm. A detailed statistical assessment of the grain size before and after imprint is shown in the supporting information (**Figure S1**).

The desired thickness of the perovskite layer is subject to design considerations of planar optical waveguides based on $MAPbBr_3$ (**Figure S2**). Accordingly, a single TE0 mode would be supported for perovskite layers with an initial thickness of 60-200 nm, which after imprinting of the grating results in a height of the hills of 110-250 nm. For thicker layers the onset of a second mode (TE1) is found (**Figure S2**).

To better analyze the effect of thermal NIL on the crystal structure of the perovskite, we studied the X-ray diffraction of the as-cast and imprinted layer, respectively. The corresponding diffractograms show dominating signals due to the 100 and 200 planes of the cubic $MAPbBr_3$ structure in agreement with the literature.[19] These prevailing reflections indicate the preferred a-axis orientation of the crystals in the layers. The 100 and 200 peaks are substantially more intense in the re-crystallized imprinted samples compared to the pristine ones. This result can be understood if we compare the cross-section SEM micrographs of the pristine and imprinted layers (insets of **Figure 1a** and **Figure 1e**, respectively). While the pristine layers show some notable inhomogeneity also in vertical direction (i.e. normal to the sample surface), the crystals extend over the entire layer thickness in the imprinted sample. Note, this becomes even more obvious in **Figure 2d**, below. As such, we interpret the more intense XRD reflection peaks as

a result of the improved crystallinity in the imprinted layers. Note, in the as-cast layers we identify two peaks labelled with (*) and (+), that cannot be associated with the $MAPbBr_3$ perovskite or $PbBr_2$.[20, 21] These peaks are absent in the imprinted layers. The positions of these peaks agree with reports on diffraction peaks of lead acetate and may thus indicate the presence of some precursor traces in the pristine layers.[22]

To analyze the concomitant impact of pressure and temperature on $MAPbBr_3$ thin films in more depth, we have used a flat stamp to better identify the structural changes inferred by the planar hot pressing (PHP) process, schematically shown in **Figure 2a**. The temperature in this particular example was 150°C but otherwise the protocol followed that outlined in **Figure 1c**. Note, we typically did not see substantial variation in the range of 100-150°C. Atomic force microscopy (AFM) has been used to study the surface morphology of the pristine and the hot pressed layer, respectively (**Figure 2b,c**). The as-cast $MAPbBr_3$ layers are very rough (rms roughness: 46 nm), which is a common finding for spin coated $MAPbBr_3$.[23, 24] Most strikingly, these initially very rough layers are dramatically flattened by the PHP process. The initial assembly of relatively small crystallites is transformed to a dense tiling of large crystals with lateral dimensions on the order of 10 µm. Most remarkably, the surface roughness of the large crystal grains is as low as 0.6 nm (rms). This residual roughness is identical to that found for the flat silicon stamp. An SEM image of the cross section reveals that the individual crystals indeed extend down to the substrate (**Figure 2d**). A notable difference between pristine and PHP layer is the substantially more intense XRD peaks of the PHP perovskite and a significantly increased environmental stability of the PHP layers (**Figure S3**). Earlier reports have evidenced that $MAPbI_3$ layers with larger crystal grains were more stable upon exposure to ambient air.[25]

A further direct effect of the flattening and thus the reduced scattering is evidenced in the optical reflectance spectra of the pristine and the PHP layers (**Figure S4**, Supporting

Information). In the sub-bandgap region ($\lambda > 630$ nm), where the absorption due the perovskite is absent, the ratio of diffuse reflectance (R_{diff}) and total reflectance (R_{total}) for the pristine and the flattened sample is 65% and 26%, respectively.

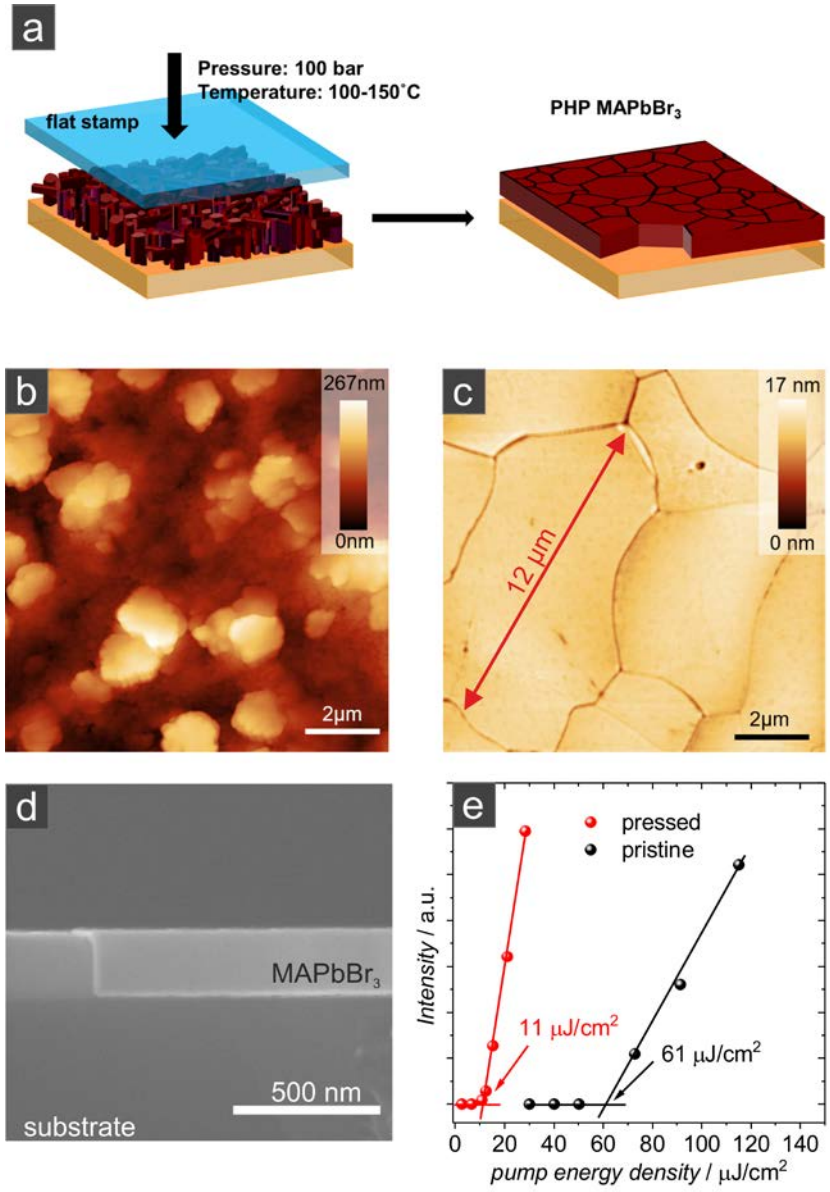

Figure 2. (a) Principle of the planar hot pressing (PHP) process using a flat stamp for the imprint procedure. AFM image of a (b) pristine and (c) PHP $MAPbBr_3$ layer. (d) SEM cross sectional image of a PHP $MAPbBr_3$ layer on a Si substrate. (e) Comparison of the output characteristics of a pristine and PHP $MAPbBr_3$ layer upon optical pumping with increasing the energy density. The threshold for the onset of amplified spontaneous emission (ASE) is marked.

As amplified spontaneous emission (ASE) is an important pre-requisite for lasing, we studied the ASE characteristics of pristine and PHP $MAPbBr_3$ layers upon optical excitation with a pulsed laser (λ = 532 nm, a pulse duration: ~ 0.3 ns, and a repetition rate of 1 kHz). In a striking difference, the threshold for the onset of ASE in the flattened PHP $MAPbBr_3$ layers is 11 $\mu J/cm^2$, substantially lower than that found in the pristine layers (61 $\mu J/cm^2$). The corresponding emission spectra below and above the ASE threshold are exemplary shown in **Figure S5** (Supporting information). The substantially reduced ASE threshold in the flattened PHP $MAPbBr_3$ layers can be related to the significantly reduced losses due to scattering.

In the following, we study the $MAPbBr_3$ films with imprinted DFB grating (**Figure 1**) upon optical excitation. The theoretical framework of DFB lasers has been published by Kogelnik and Shank.[26] Essentially, the Bragg wavelength for second-order DFB resonators can be determined by $\lambda_{Bragg} = n_{eff} \times \Lambda$, where n_{eff} denotes the effective refractive index of the guided optical mode. Λ is the period of the DFB grating, i.e. 300 nm in our samples.

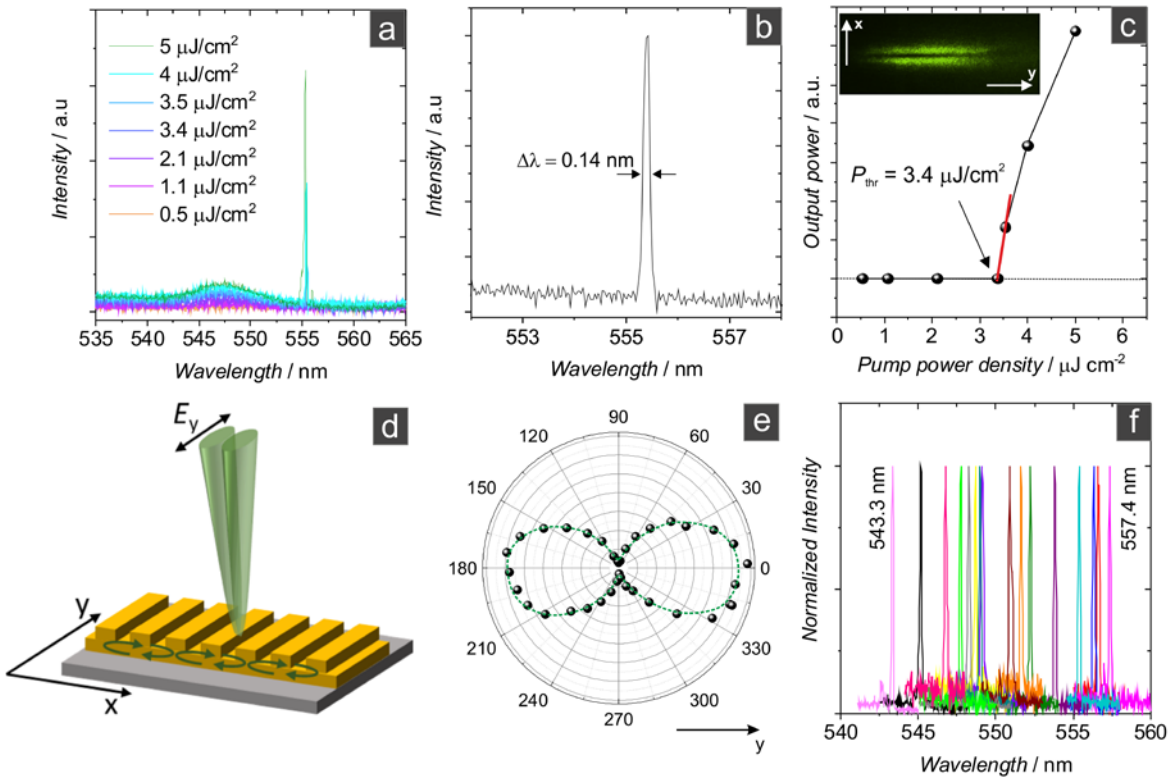

Figure 3. (a) Emission spectra upon optical pumping with increasing energy density 0.5-5 μJ/cm^2. (b) Emission spectrum of the laser measured with high spectral resolution. (c) Output power vs. excitation density demonstrating a clear threshold behavior. The inset show the dual lobed far field emission pattern above threshold. (d) Schematic of the DFB laser with assignment of directions and a sketch of the laser emission as a result of first order diffraction normal to the sample surface. (e) Polarization characteristics of the laser emission. (f) Tunability of the DFB laser wavelength as we vary the excitation spot on the sample. Here, local variations of the layer thickness infer a variation of the effective refractive index n_{eff} (c.f. **Figure S4**).

Representative spectral emission characteristics of the $MAPbBr_3$ DFB laser upon increasing the optical excitation density from 0.5-5 μJ/cm^2 are shown in **Figure 3a**. At an excitation density

in excess of 3.4 μJ/cm^2, a sharp emission line at λ = 555.3 nm appears. The determined width of this emission line is Δλ = 0.14 nm, limited by the resolution of our spectrometer (**Figure 2b**). The narrow spectrum of the laser emission is clearly different from the ASE spectrum, which is peaked at 550.7 nm and is significantly broader (spectral width: 2.5 nm) (**Figure S5**, Supporting Information). In agreement with the collapse of the width of the emission spectrum, the output power shows an abrupt increase for excitation levels above a threshold of 3.4 μJ/cm^2, which is the characteristic behavior for the transition from spontaneous emission to lasing (**Figure 3c**). It has to be noted, that for a second-order DFB laser, the emission can be detected normal to the sample surface. The corresponding far-field characteristics above threshold are shown in the inset of **Figure 3c**, featuring a highly astigmatic dual-lobed pattern, which is typical for the emission of complex coupled DFB lasers based on linear grating resonators with strong diffractive out-coupling.[27] The corresponding schematic of the DFB laser is shown in **Figure 3d**. Note, the two lobes in the far-field arise as a Fourier transform of the near-field characteristics of the dominating anti-symmetric resonator mode, as discussed in detail by Noll et al..[28] If desired, a single lobed emission could be achieved by introducing a phase shift of π. Aside from the characteristic far-field pattern, the laser emission shows a pronounced linear polarization (**Figure 3e**), with the electrical field-vector parallel to the DFB grating (*y*-direction). Finally, **Figure 3f** shows the wavelength tunability of the laser emission (between 543.3-557.4 nm) as a result of the varied effective refractive index n_{eff}. Note, the local variation of n_{eff} is a result of the thickness inhomogeneity of the spin-coating process used for the deposition of the pristine $MAPbBr_3$ layer. The increase of n_{eff} with increasing the layer thickness has been discussed above (**Figure S1**). An increase of n_{eff} with increasing the thickness of the $MAPbBr_3$ waveguide layer directly infers a red-shift of the lasing wavelength.

In summary, the first DFB lasers based on $MAPbBr_3$ thin films have been realized. Linear Bragg gratings were created by direct thermal nanoimprint into thin films of methyl-ammonium

lead bromide. The imprinted resonator structures provided high quality resonators. As notable effect of the imprinting process, aside from the pattering, we achieved a substantial flattening of an initially very rough polycrystalline layer to a layer with large crystals on the order of tens of microns with a surface roughness of 0.6 nm. A significantly lowered threshold for the onset of amplified spontaneous emission results from the reduced scattering. In optically pumped DFB laser structures, very low lasing thresholds of 3.4 $\mu J/cm^2$ are achieved. Low lasing threshold levels are essential on the way to the first electrically operated perovskite laser diode. Beyond lasers, we expect that our results will likewise influence perovskite research on other (opto-)electronic devices, e.g. LEDs and solar cells.

Methods

Pristine $MAPbBr_3$ layer preparation

Lead acetate trihydrate (purity 99.999%) (Sigma-Aldrich) and Methylammonium Bromide (Dyesol) were dissolved in anhydrous DMF (purity 99.9%) (Sigma-Aldrich) with a 3:1 molar ratio of CH_3NH_3Br:$Pb(Ac)_2$, (stirred and heated over night at 60°C in nitrogen environment). We used Borofloat glass substrates for the lasers and silicon wafers for SEM characterization. All substrates were cleaned as reported previously.[17] The perovskite layers were prepared by spin-coating the precursor solution at 5,000 r.p.m, for 3 min. After spin-coating, the films were annealed on a hotplate at 100°C for 2 min.

Thermal Nanoimprint / Hot pressing

Thermal nanoimprint and planar hot pressing experiments were performed in a parallel plate based imprint system.[29] The imprint procedure is shown in **Figure 1c**, taking the example of an imprint temperature of 100°C. During heat-up of the system to the processing temperature, which, in this case, takes about 10 min, a pre-pressure of 25 bar is applied. When the imprint

temperature is reached the pressure is raised to 100 bar. After an imprint time of 3 min the system is cooled down and the pressure is released slowly as soon as a temperature is below 30°C. Imprint temperatures of 100°C and 150°C were used. The stamp used for nanoimprint features 150 nm lines and spaces. The height of the ridges is 150 nm; it is made from Ormostamp (microresist, Berlin) and provided with an anti-sticking layer.[30, 31] For planar hot pressing the stamp was un-patterned silicon, again provided with an anti-sticking layer. The procedure for planar hot pressing was similar to the imprint procedure; the pre-pressure used was 100 bar and the pressing time was increased to 30 min.

Characterization of materials and devices

X-ray diffraction (XRD) was measured using a Cu-$K_{\alpha 1,2}$-source with Ni filter in a Bruker D2 Phaser system. Alternatively, an Philips X'Pert Pro MPD system with a monochromatic Cu-$K_{\alpha 1,2}$-source has been used. For XRD, we used layers on glass substrates. For the SEM studies layers on Si substrates were investigated using a Philips XL30S FEG microscope with a field emission cathode. AFM measurements were conducted with a Bruker Innova system in tapping mode (tip: RTESPA-300; tip radius: < 12 nm).

The diffuse reflectance of the pristine and flattened films was measured with an integrating sphere (RTC-060-SF Labsphere) in double beam mode using a fiber-coupled collimated LED light source (MWWHF2, Thorlabs) with an output power of about 16 mW. The spectra in the range from 430 to 670 nm were recorded with an integration time of 8 s and an optical resolution of around 1.9 nm (spectrometer USB 2000+XR1-ES, Ocean Optics). Luminescence of the films (below 630 nm) was blocked with an optical filter.

For photoluminescence (PL) measurements, we used laser diode for excitation (λ = 457 nm, power density 0.4 W/cm^2). The samples were kept in ambient air. The PL spectra were detected using a monochromator (Princeton Instruments, Acton SP2500, gratings: 300 lines/mm and 1200 lines/mm) and a thermoelectrically cooled charge coupled device (CCD) camera

(Princeton Instruments). The perovskite laser samples were optically pumped by a frequency-doubled diode-pumped solid state laser (PowerChip NanoLaser, TEEM Photonics, France) with λ = 532 nm, a pulse duration ~ 0.3 ns, and a repetition rate of 1 kHz. The excitation spot had an area of 0.3 mm^2. The excitation density has been varied by a neutral density filter wheel. The power of the pump laser has been measured with a thermal sensor head (S470C, ThorLabs).

The far field emission characteristics of the DFB lasers were recorded by using a sand-blasted glass screen at a distance of about 2 cm to the sample surface and a Si CMOS camera (DCC1545M**,** ThorLabs) with a 25 mm fixed focal length objective equipped and an optical filter to suppress the light of the pump laser.

Supporting Information

Supporting Information is available from the Wiley Online Library or from the author.

Acknowledgements

We want to thank Dr. Irma Päschke (Lehrstuhl für Neue Fertigungstechnologien und Werkstoffe, University of Wuppertal) and Prof. Dirk Lützenkirchen-Hecht (Condensed Matter Physics, University of Wuppertal) for the support with the XRD measurements. The authors acknowledge the German Federal Ministry for Education and Research (Grant No. 13N13819) for financial support. P.G. acknowledges funding by the Emmy-Noether-Programm of the DFG (Deutsche Forschungsgemeinschaft). This project has received funding from the European Research Council (ERC) under the European Union's Horizon 2020 research and innovation programme (grant agreement No. 637367).

References

[1] W. S. Yang, B.-W. Park, E. H. Jung, N. J. Jeon, Y. C. Kim, D. U. Lee, S. S. Shin, J. Seo, E. K. Kim, J. H. Noh, S. I. Seok, *Science* **2017**, *356*, 1376.

[2] B. R. Sutherland, E. H. Sargent, *Nat Photon* **2016**, *10*, 295.

[3] S. D. Stranks, H. J. Snaith, *Nat Nano* **2015**, *10*, 391.

[4] Z. Xiao, R. A. Kerner, L. Zhao, N. L. Tran, K. M. Lee, T.-W. Koh, G. D. Scholes, B. P. Rand, *Nat Photon* **2017**, *11*, 108.

[5] N. Wang, L. Cheng, R. Ge, S. Zhang, Y. Miao, W. Zou, C. Yi, Y. Sun, Y. Cao, R. Yang, Y. Wei, Q. Guo, Y. Ke, M. Yu, Y. Jin, Y. Liu, Q. Ding, D. Di, L. Yang, G. Xing, H. Tian, C. Jin, F. Gao, R. H. Friend, J. Wang, W. Huang, *Nat Photon* **2016**, *10*, 699.

[6] G. Xing, N. Mathews, S. S. Lim, N. Yantara, X. Liu, D. Sabba, M. Grätzel, S. Mhaisalkar, T. C. Sum, *Nat Mater* **2014**, *13*, 476.

[7] F. Deschler, M. Price, S. Pathak, L. E. Klintberg, D.-D. Jarausch, R. Higler, S. Hüttner, T. Leijtens, S. D. Stranks, H. J. Snaith, M. Atatüre, R. T. Phillips, R. H. Friend, *The Journal of Physical Chemistry Letters* **2014**, *5*, 1421.

[8] B. R. Sutherland, S. Hoogland, M. M. Adachi, C. T. O. Wong, E. H. Sargent, *Acs Nano* **2014**, *8*, 10947.

[9] S. Chen, K. Roh, J. Lee, W. K. Chong, Y. Lu, N. Mathews, T. C. Sum, A. Nurmikko, *Acs Nano* **2016**, *10*, 3959.

[10] Y. Jia, R. A. Kerner, A. J. Grede, A. N. Brigeman, B. P. Rand, N. C. Giebink, *Nano Lett* **2016**, DOI: 10.1021/acs.nanolett.6b01946.

[11] H. Zhu, Y. Fu, F. Meng, X. Wu, Z. Gong, Q. Ding, M. V. Gustafsson, M. T. Trinh, S. Jin, X. Y. Zhu, *Nat Mater* **2015**, *14*, 636.

[12] Y. Fu, H. Zhu, C. C. Stoumpos, Q. Ding, J. Wang, M. G. Kanatzidis, X. Zhu, S. Jin, *Acs Nano* **2016**, *10*, 7963.

[13] Y. Fu, H. Zhu, A. W. Schrader, D. Liang, Q. Ding, P. Joshi, L. Hwang, X. Y. Zhu, S. Jin, *Nano Lett* **2016**, *16*, 1000.

[14] D. Lyashenko, A. Perez, A. Zakhidov, *physica status solidi (a)* **2017**, *214*, n/a.

[15] G. Niu, W. Li, F. Meng, L. Wang, H. Dong, Y. Qiu, *Journal of Materials Chemistry A* **2014**, *2*, 705.

[16] D. A. Egger, L. Kronik, *The Journal of Physical Chemistry Letters* **2014**, *5*, 2728.

[17] N. Pourdavoud, S. Wang, A. Mayer, T. Hu, Y. Chen, A. Marianovich, W. Kowalsky, R. Heiderhoff, H.-C. Scheer, T. Riedl, *Adv Mater* **2017**, *29*, 1605003.

[18] H. Wang, R. Haroldson, B. Balachandran, A. Zakhidov, S. Sohal, J. Y. Chan, A. Zakhidov, W. Hu, *Acs Nano* **2016**, *10*, 10921.

[19] M. I. Saidaminov, A. L. Abdelhady, B. Murali, E. Alarousu, V. M. Burlakov, W. Peng, I. Dursun, L. Wang, Y. He, G. Maculan, A. Goriely, T. Wu, O. F. Mohammed, O. M. Bakr, *Nat Commun* **2015**, *6*, 7586.

[20] M. C. M. Morris, Howard F.; Evans, Eloise H.; Paretzkin, Boris; Hubbard, Camden R.; Carmel, Simon J., Washington D.C.. (digital.library.unt.edu/ark:/67531/metadc13209/: accessed April 25, 2017) 1980.

[21] H. Kusumoto, T. Kaito, S.-i. Yanagiya, A. Mori, T. Inoue, *J Cryst Growth* **2005**, *277*, 536.

[22] F. J. Martínez-Casado, M. Ramos-Riesco, J. A. Rodríguez-Cheda, F. Cucinotta, E. Matesanz, I. Miletto, E. Gianotti, L. Marchese, Z. Matěj, *Inorganic Chemistry* **2016**, *55*, 8576.

[23] H. Cho, S.-H. Jeong, M.-H. Park, Y.-H. Kim, C. Wolf, C.-L. Lee, J. H. Heo, A. Sadhanala, N. Myoung, S. Yoo, S. H. Im, R. H. Friend, T.-W. Lee, *Science* **2015**, *350*, 1222.
[24] J. H. Heo, D. H. Song, S. H. Im, *Adv Mater* **2014**, *26*, 8179.
[25] H.-J. Yen, P.-W. Liang, C.-C. Chueh, Z. Yang, A. K. Y. Jen, H.-L. Wang, *Acs Appl Mater Inter* **2016**, *8*, 14513.
[26] H. Kogelnik, C. V. Shank, *J Appl Phys* **1972**, *43*, 2327.
[27] M. Kasraian, D. Botez, *Appl Phys Lett* **1995**, *67*, 2783.
[28] R. J. Noll, S. H. Macomber, *Ieee J Quantum Elect* **1990**, *26*, 456.
[29] A. Mayer, S. Moellenbeck, K. Dhima, S. Wang, H.-C. Scheer, *J Vac Sci Technol B* **2011**, *29*, 06FC13.
[30] C. Steinberg, K. Dhima, D. Blenskens, A. Mayer, S. Wang, M. Papenheim, H.-C. Scheer, J. Zajadacz, K. Zimmer, *Microelectron Eng* **2014**, *123*, 4.
[31] M. Papenheim, C. Steinberg, K. Dhima, S. Wang, H.-C. Scheer, *J Vac Sci Technol B* **2015**, *33*, 06F601.